Lyman-Alpha Emission from K and M Dwarfs: Intrinsic Profiles, Variability, and Flux in the Habitable Zone

Sarah Peacock,[1,2] Travis S. Barman,[3] R. O. Parke Loyd,[4] Adam C. Schneider,[5] Allison Youngblood,[2] Kenneth G. Carpenter,[2] and Evgenya L. Shkolnik[6]

[1] University of Maryland, Baltimore County, MD 21250, USA
[2] NASA Goddard Space Flight Center, Greenbelt, MD 20771, USA
[3] University of Arizona, Lunar and Planetary Laboratory, 1629 E University Boulevard, Tucson, AZ 85721, USA
[4] Eureka Scientific, Inc., 2452 Delmer Street Suite 100, Oakland, CA 94602-3017, USA
[5] US Naval Observatory, Flagstaff Station, 10391 West Naval Observatory Road, Flagstaff, AZ 86002-8521, USA
[6] School of Earth and Space Exploration, Arizona State University, Tempe, AZ 85281, USA

ABSTRACT

Lyman-α (Lyα) is the most prominent ultraviolet emission line in low-mass stars, playing a crucial role in exoplanet atmospheric photochemistry, heating, and escape. However, interstellar medium (ISM) absorption typically obscures most of the Lyα profile, requiring reconstructions that introduce systematic uncertainties. We present intrinsic Lyα profiles for 12 high radial velocity K and M dwarfs, where Doppler shifting minimizes ISM contamination, allowing direct measurements of $\sim$50–95% of the line flux. Our sample spans the K-to-M spectral transition, enabling us to constrain the dependence of self-reversals in Lyα emission profiles on effective temperature (T_{eff}). The depth of self-reversal, driven by non-local thermodynamic equilibrium (LTE) effects, decreases with decreasing T_{eff}, with M dwarfs exhibiting little to none. Two stars, Ross 1044 and Ross 451, were observed over multiple days, revealing $\sim$20% Lyα variability confined to the line core - implying that studies relying on reconstructions may underestimate temporal variability. We find strong correlations between Lyα flux, peak-to-trough ratio, and hydrogen departure coefficients with T_{eff}, providing empirical constraints for stellar atmosphere models. A comparison of Lyα flux in the habitable zone shows measured values for high radial velocity stars less than the reconstructed values for the rest of the sample, likely due to the older ages of the high-RV stars and/or overestimated reconstructed fluxes due to model deficiency (e.g., neglecting self-reversal). Our results establish an empirical foundation for Lyα emission in K and M dwarfs, reducing uncertainties in reconstructions and improving models of stellar UV emission relevant to exoplanetary studies.

Keywords: Stellar astronomy (1583) — Low-Mass Stars (2050) — Stellar Chromospheres (230) — Stellar Activity (1580) — Ultraviolet Astronomy (1736)

1. INTRODUCTION

The H I Lyman-α (Lyα; λ1215.67 Å) transition is the dominant ultraviolet (UV) emission feature in low-mass stars, with the intrinsic line flux estimated to contribute approximately 37%–75% of the total 1150–3100 Å flux from most late-type stars (K. France et al. 2013). This emission plays a crucial role in stellar atmosphere modeling: the ionization balance of H I/H II in the outer stellar layers influences the overall atmospheric structure, and the line core is highly sensitive to the chromosphere and transition region, where non-radiative heating mechanisms remain poorly understood (C. I. Short & J. G. Doyle 1997; S. Peacock et al. 2022). Additionally, Lyα radiation is a key driver of photodissociation in exoplanet atmospheres, breaking down molecules such as H_2O and CH_4 (e.g., S. Rugheimer et al. 2015). Since Lyα controls atmospheric photochemistry, accurate estimates of its intrinsic flux are essential for assessing planetary habitability and interpreting atmospheric observations. Reconstructed Lyα fluxes have been widely used to establish correlations with other spectral emission lines (J. L. Linsky et al. 2013; A. Youngblood et al. 2017; K. Melbourne et al. 2020), broadband UV photometry (E. L. Shkolnik et al. 2014), and X-ray fluxes (J. L. Linsky et al.

2020). These correlations are often employed to assess the life-supporting potential of different stellar types (M. Cuntz & E. F. Guinan 2016), but systematic offsets may arise due to assumptions made in Lyα reconstructions.

Despite its importance, direct measurements of the intrinsic Lyα line profile, flux, and variability are challenging due to severe absorption by neutral hydrogen in the interstellar medium (ISM) and contamination from geocoronal airglow, which affect over 99% of observations. Standard approaches rely on reconstruction techniques that introduce uncertainties through assumptions about the intrinsic line shape and ISM properties along the line of sight (A. Youngblood et al. 2016; D. J. Wilson et al. 2022; A. Sandoval et al. 2023). While significant effort goes into these reconstructions, they depend on assumptions about the shape of the line core and the structure of the ISM. A. Youngblood et al. (2016) estimate that both could independently yield ∼30% inaccuracies, while A. Sandoval et al. (2023) finds that in extreme cases, Lyα flux estimates can be off by factors of 3–5. Additionally, D. J. Wilson et al. (2022) identified a 2× systematic uncertainty in the reconstruction process by comparing reconstructions of the M dwarf component of EG UMa, a tight white dwarf-M dwarf binary, performed at different orbital phases. Mg II self-reversed emission-line profiles provide some constraints on the Lyα line core, but differences between the two lines - such as formation temperatures - are significant enough that Mg II cannot serve as a direct template for Lyα reconstructions (A. Youngblood et al. 2022).

Recent observations with the Space Telescope Imaging Spectrograph (STIS) onboard the Hubble Space Telescope (HST) have provided new insights by directly measuring intrinsic Lyα profiles in six M and K-type stars with exceptionally large radial velocities ($|RV| > 85$ km s^{-1}), which Doppler shift the Lyα emission away from these contaminating sources (A. C. Schneider et al. 2019; A. Youngblood et al. 2022). These observations reveal that self-reversal in the Lyα line core is common among low-mass stars and that the depth of self-reversal correlates with surface gravity, with lower-mass stars exhibiting weaker self-reversals. Previous PHOENIX stellar atmosphere models underpredicted the Lyα core strength for these stars, highlighting the need for improved microphysics in the upper atmosphere models (S. Peacock et al. 2022). The self-reversal in Lyα arises from non-local thermodynamic equilibrium (non-LTE) effects, as the line forms over extensive depths in the chromosphere and transition region where collisional processes become less dominant, allowing the line source function to depart from the Planck function. Modeling the Lyα lines of these stars demonstrated the sensitivity of the core flux to departures from LTE in the $n = 2$ state of H I at the boundary between the chromosphere and transition region. These departure coefficients indicate missing or incorrect opacities in the models, requiring adjustments to the minimum values set in these layers to reproduce observed Lyα profiles.

These findings have significant implications for reconstructing Lyα emission in stars where direct measurements remain infeasible. Self-reversal in Lyα profiles must be accounted for to avoid overestimations of intrinsic flux by as much as 60%–100% for G and K dwarfs and 40%–170% for M dwarfs (A. Youngblood et al. 2022). Moreover, improved Lyα modeling directly translates to better predictions of the EUV spectrum (e.g., J. L. Linsky et al. 2013; S. Peacock et al. 2019; J. L. Linsky & S. Redfield 2024), which is crucial for understanding atmospheric escape and photochemistry in exoplanets.

The results from A. Youngblood et al. (2022) and S. Peacock et al. (2022) reaffirm that the depth of self-reversal in Lyα increases with earlier spectral type; however, small sample sizes have limited precise characterization of how the line profile changes with uniform temperature steps of less than 1000 K. In this paper, we expand on these works with new HST STIS observations, adding six additional M and K stars for which >85% of the intrinsic Lyα flux can be directly measured, all with absolute radial velocities exceeding 100 km s^{-1}. These observations double the sample of low-mass stars for which Lyα can be measured directly, uniformly sampling stars with $T_{\rm eff}$ from 3400 to 5500 K in steps of approximately 500 K. By increasing the number of high-RV targets with directly observed Lyα profiles and refining stellar atmosphere models, this study enhances our ability to accurately predict stellar Lyα fluxes. These improvements are essential for interpreting exoplanetary atmospheres and assessing habitability, particularly for planets orbiting low-mass stars where Lyα dominates the high-energy radiation environment.

2. OBSERVATIONS AND REDUCTIONS

We observed six low-mass K and M stars—HD 64090 (K0), HD 134439 (K1), HD 134440 (K2), HIP 117795 (K8), Ross 451 (M0), and L 802-6 (M3)—between March 26, 2022, and January 19, 2023, using HST/STIS (Table 1). These targets were selected based on their RVs, as our goal was to observe Lyα emission lines shifted outside the regions strongly affected by ISM absorption and geocoronal emission. We identified low-mass stars ($T_{\rm eff} \leq 5500$ K) in the *Gaia* DR2 catalog[7] with absolute RVs greater than 100 km s^{-1}. This threshold corresponds to a wavelength shift of

Table 1. Observations

Star	Observation Date	Orbits	Exposure Time (s)	SNR_{wing}	SNR_{core}
HD 64090	2022-Mar-26	1	1614	5.0	9.2
HD 134439	2022-Jul-04	2	4324	5.8	13.9
HD 134440	2202-Jul-07	2	4324	4.6	12.8
Ross 451	2022-Oct-01	3	7882	4.2	6.3
Ross 451	2022-Oct-02	3	7882	$\cdots$	$\cdots$
Ross 451	2022-Oct-03	3	7882	$\cdots$	$\cdots$
HIP 117795	2022-Oct-15	3	7733	4.6	11.8
L 802-6	2023-Jan-19	3	6840	5.4	6.2

NOTE—Observations of targets from HST-GO-16646. All observations were taken with STIS/G140M centered at 1222 Å. The right-most columns give the SNR per resolution element for the coadded spectrum in the wing (0.6 Å from the line core, on the side furthest from the ISM absorption) and nearest to the core of the Lyα line. For Ross 451, a single SNR value is listed because all visits were combined into one final spectrum.

$\approx$0.4 Å, though the exact RV required to shift the Lyα peak out of the contaminated wavelength range varies with the line of sight to each star. Different sight lines have ISM absorbers at different RVs, usually between ± 30 km s^{-1} (S. Redfield & J. L. Linsky 2008).

These observations, obtained as part of HST GO Program 16646 (DOI: 10.17909/bx2r-na24), spanned a total of 22 orbits. For each target, we used the STIS/G140M grating with the $52'' \times 0''.1$ slit, centered at 1222 Å, to capture the Lyα wavelength region.

During the data reduction process, we identified extraction issues in the standard pipeline for some targets (Ross 451, HIP 117795, and L 802-6), where the spectral trace was not properly located by the automated calSTIS pipeline. To correct this, we manually located the spectral traces in the flat-fielded images (flt files), then forced extraction of the 1D spectrum at this location with calSTIS. To maintain consistency, we manually identified the trace location for all spectra. In the manual extractions, we moved the background estimation regions to an offset of 10 pixels above and below the spectral trace with widths of 20 pixels. Calibration reference files were those current as of 2023 March 10. Additionally, a two-orbit visit for HIP 117795 on October 14 failed due to user error in the selection of the acquisition aperture (F25ND5 was used in place of the intended F25ND3). As a result, we only used the visit from October 15 for this star.

For targets with multiple observations, we coadded the background-subtracted spectra by first interpolating them onto a common wavelength grid with $\Delta \lambda = 0.05$ Å and then performing an exposure-time-weighted average. The signal-to-noise ratio (SNR) per resolution element in the wings and nearest to the core of Lyα for each star is listed in Table 1, with values ranging from 4.2–5.8 in the wings and 6.2–13.9 near the core. The loss of two orbits for HIP 117795 did not significantly impact the data quality, as the SNR near the core remained relatively high at 11.8. Ross 451 and L 802-6 have the lowest core SNRs ($\sim$6), due to their lower radial velocities ($\sim$100–150 km s^{-1}), which provided a smaller Doppler shift away from contaminating sources compared to the other four stars (> 230 km s^{-1}).

Figure 1 presents the coadded spectra for our six newly observed targets, alongside archival spectra of six additional low-mass stars with high radial velocities from A. C. Schneider et al. (2019) (Ross 825, Ross 1044) and A. Youngblood et al. (2022) (HD 191408, GL 411, Barnard's Star, and Kapteyn's Star). The Schneider et al. stars were observed with HST/STIS using the G140M grating, while the Youngblood et al. stars were observed with HST/STIS using the E140M echelle mode. These archival data are incorporated into our analysis to expand coverage in stellar parameter space and to strengthen our comparison across effective temperature. The full sample of 12 stars spans T_{eff} from 3300 to 5500 K in steps of 40 to 500 K (Table 2) and reveals nearly complete line profiles, with subtle core reversals that

---

[7] The *Gaia* DR2 catalog contains more than 7.2 million radial velocity measurements, and the Gaia EDR3 release did not include new radial velocity data at the time of the observing proposal submission.

¹²¹ become more pronounced in hotter stars. Further details of additional components in Figure 1 are explained in Section
¹²² 3.

3. MODELING INTRINSIC Lyα PROFILES WITH PHOENIX

¹²³

¹²⁴ The high radial velocities of the 12 stars shift the Lyα line by 0.34 to 1.38 Å, revealing 47% to 95% of the intrinsic
¹²⁵ profiles (Table 3) that would otherwise be mostly obscured by the ISM. To ensure a fair comparison between models
¹²⁶ and observations, we applied the appropriate ISM absorption for each target's line of sight. We computed ISM
¹²⁷ transmittance curves for each target by performing a reconstruction following methods from A. Youngblood et al.
¹²⁸ (2022). Briefly, we forward-modeled the observed spectrum with an intrinsic stellar emission profile and an ISM
¹²⁹ absorption profile using lyapy (A. Youngblood & E. R. Newton 2025). The product of the two profiles is convolved
¹³⁰ with the instrument line spread function. We assume a self-reversed Voigt profile for the stellar emission and a single
¹³¹ absorption component for the ISM. The optical depth of the H I and D I lines are modeled as Voigt profiles. For the
¹³² subsequent analysis, we solely retain the ISM absorption profiles.

¹³³ To reproduce the intrinsic Lyα profiles for the complete set of 12 stars, we computed models using the PHOENIX
¹³⁴ atmosphere code (P. H. Hauschildt 1993; P. H. Hauschildt & E. Baron 2006; E. Baron & P. H. Hauschildt 2007),
¹³⁵ following the methodology of S. Peacock et al. (2022). For each modeled star, we constructed photospheric structures
¹³⁶ based on literature values for effective temperature ($T_{\rm eff}$), mass ($M_\star$), surface gravity ($\log(g)$), and metallicity ([Fe/H])
¹³⁷ (Table 2). To these photospheres, we added chromospheric and transition region layers modeled as linear temperature
¹³⁸ rises as a function of log(column mass), reaching a maximum temperature of 2×10^5 K. This upper limit exceeds
¹³⁹ the temperature range in which Lyα forms ($\approx 2 \times 10^3 - 8 \times 10^4$ K) and is consistent with our previous analysis. The
¹⁴⁰ temperature at the top of each chromosphere, where hydrogen becomes fully ionized and the atmosphere becomes
¹⁴¹ thermally unstable, ranges from 7000 to 8000 K. In S. Peacock et al. (2022), we confirmed that assuming a linear
¹⁴² temperature rise with log(column mass) when modeling the stellar chromosphere yields spectra that best match UV
¹⁴³ observations. Additionally, we found that smoothing the temperature structure at the chromosphere-transition region
¹⁴⁴ boundary has a negligible effect on the computed UV spectrum, including the Lyα profile.

¹⁴⁵ The Lyα profiles were computed assuming Voigt functions. We included line blanketing in the background opacities,
¹⁴⁶ computed Lyα with partial frequency redistribution, and incorporated the same robust set of species computed in
¹⁴⁷ non-local thermodynamic equilibrium (non-LTE) as in S. Peacock et al. (2022). We used a microturbulent velocity of
¹⁴⁸ 2 km s^{-1} in the photosphere and a velocity gradient in the chromosphere and transition region set as a fraction of the
¹⁴⁹ local sound speed ($0.35 \times v_{sound}$), with a maximum velocity capped at 10 km s^{-1}.

¹⁵⁰ For each star, we computed a grid of 72 distinct upper atmosphere models, varying the location and thickness of
¹⁵¹ both the chromosphere and transition region using three free parameters: (1) the base of the chromosphere, (2) the
¹⁵² top of the chromosphere, and (3) the temperature gradient in the transition region. A key difference from S. Peacock
¹⁵³ et al. (2022) is that not all stars in this study have NUV observations to provide additional empirical constraints
¹⁵⁴ on the upper atmospheric structure. Four stars (HD 191408, Kapteyn's Star, GJ 411, and Barnard's Star) have
¹⁵⁵ archival *HST*/STIS E230H spectra (with some also having additional gratings), while six others (Ross 825, Ross 1044,
¹⁵⁶ HD 64090, HIP 117795, Ross 451, and L802-6) have GALEX NUV photometry. Two additional stars (HD 134439 and
¹⁵⁷ HD 134440) are listed as having STIS G230LB observations, but the data are not publicly available. Because of this
¹⁵⁸ heterogeneity in NUV coverage and data quality across the sample, we chose to fit only the Lyα line in order to apply a
¹⁵⁹ consistent modeling approach to all 12 stars. To compare the models with observations, we applied the radial velocity
¹⁶⁰ shifts, multiplied by the appropriate ISM transmittance curves, scaled the flux by $R_\star^2/dist^2$, and then convolved the
¹⁶¹ model spectra to the observational resolution. As in S. Peacock et al. (2022), our initial model setup yielded spectra
¹⁶² that successfully reproduced the observed Lyα line widths, but severely underestimated the line core (see Appendix).

¹⁶³ The departure coefficients, which represent the ratio of non-LTE to LTE number densities, serve as proxies for
¹⁶⁴ the population of each energy level and are essential for calculating emissivity and absorption coefficients. The Lyα
¹⁶⁵ line is produced by electron transitions from the n=2 state to the ground state (n=1) in hydrogen. In S. Peacock
¹⁶⁶ et al. (2022), we showed that in our original model setup, the departure coefficient for the n=2 state drops by several
¹⁶⁷ orders of magnitude at the chromosphere-transition region boundary (also shown in Figures 9, 10, and 11 in the
¹⁶⁸ Appendix). This sharp decrease indicates a severe underprediction of the hydrogen n=2 population in this region,
¹⁶⁹ whereas observations suggest it should be much closer to the LTE population. A key finding of that study was that
¹⁷⁰ the strength of the self-reversal in the Lyα line core is highly sensitive to the minimum value set in the layers around
¹⁷¹ the chromosphere-transition region boundary. We found that manually increasing the n=2 ratio across the upper
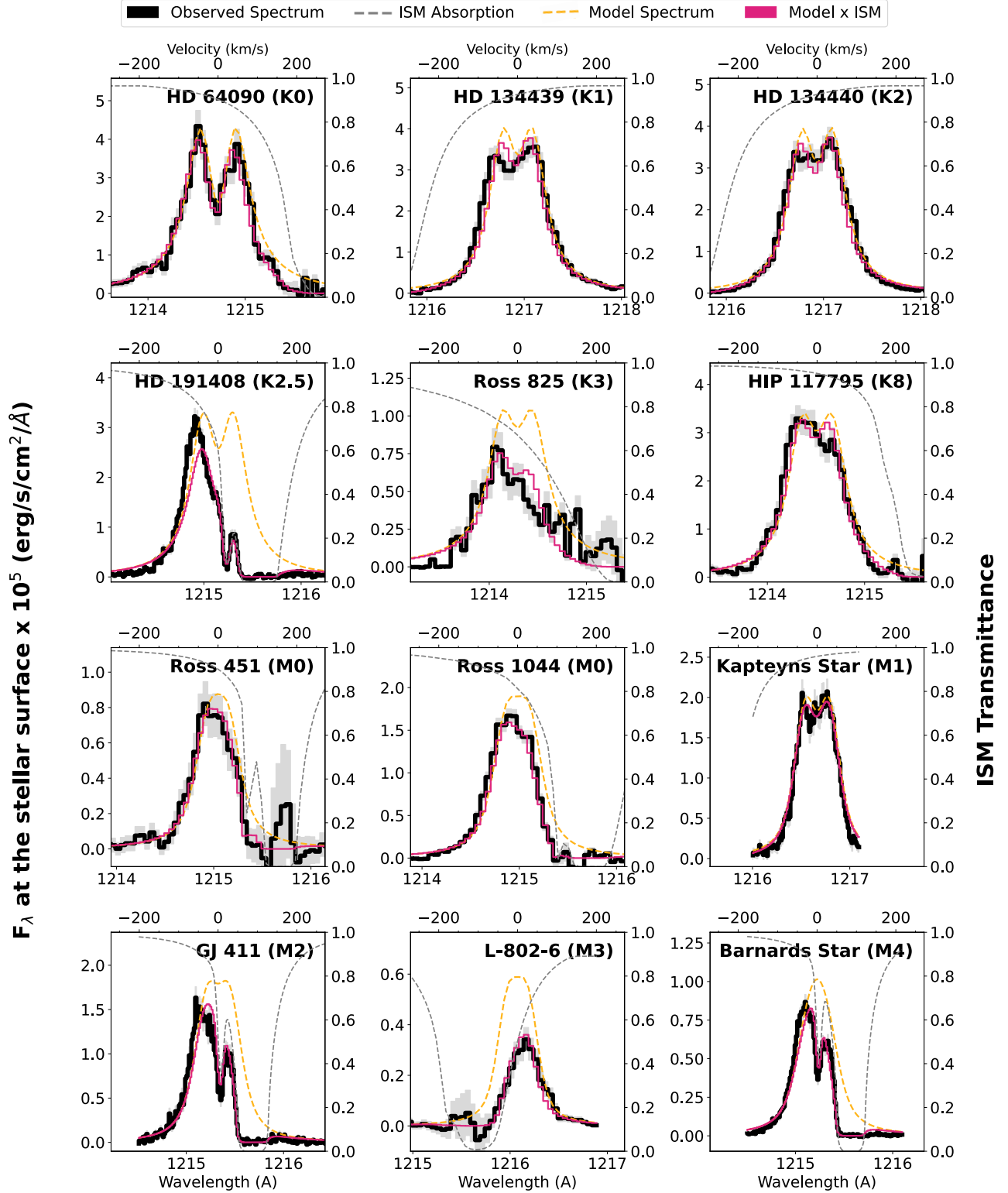
Figure 1. Lyα profiles of low-mass K and M stars with high radial velocities ($|\mathrm{RV}| > 84$ km s^{-1}) ordered by spectral type. HST/STIS observations are plotted in black, with associated errors shaded in gray. All stars were observed with the G140M grating, except for HD 191408, Kapteyn's Star, GJ 411, and Barnard's Star, which were observed with E140M. The ISM transmittance curve for each star is plotted as a gray dashed line. Intrinsic PHOENIX model profiles are plotted in yellow. The intrinsic PHOENIX model, after being multiplied by the ISM transmittance curve, is plotted in pink — this profile should match the observations. The yellow profile represents the intrinsic stellar emission before ISM absorption.

Table 2. Stellar Properties

Star	Sp. Type	$T_{\rm eff}$ (K)	$\log(g)$ (cm s^{-2})	[Fe/H]	$M_\star$ ($M_\odot$)	$R_\star$ ($R_\odot$)	[Fe/H]	Distance (pc)	$v\sin i$ (km s^{-1})	RV (km s^{-1})	Age (Gyr)
HD 64090	K0	5528 ± 35^a	4.62 ± 0.3	-1.64 ± 0.15	0.9	0.62 ± 0.04^{m}	-1.64	27.35 ± 0.02	$-0.3 - 8^{y,m}$	-234.1 ± 0.15	$6.72^{+5.6}_{-4.8}\ (ac)$
HD 134439	K1	5065 ± 72^b	4.56 ± 0.1	-1.46 ± 0.1	0.8	0.60 ± 0.01^{m}	-1.46	29.40 ± 0.01	$-0.87 - 7^{n,o}$	310.3 ± 0.2	$7.18 - 9.9^{ad,ae}$
HD 134440	K2	4796 ± 57^c	4.64 ± 0.1	-1.41 ± 0.1	0.75	0.56 ± 0.01^{m}	-1.41	29.39 ± 0.01	$-0.13 - 7^{n,o}$	311.1 ± 0.2	$6.12 - 9.4^{ad,ae}$
HD 191408	K2.5	4893 ± 49^d	4.6 ± 0.1	-0.07 ± 0.03	0.82	0.74 ± 0.17^n	-0.07	6.01 ± 0.01	$3.02 - 3.97^{p,q}$	-129.3 ± 0.1	$6.26 - 11.24^{ad,a,f}$
Ross 825	K3	4680 ± 170^e	4.75 ± 0.2	-1.28 ± 0.1	0.55	0.83 ± 0.21^o	-1.28	98.26 ± 0.18	$\cdots$	-341.2 ± 0.5	$> 10^{ag}$
HIP 117795	K8	4100 ± 150^f	4.75 ± 0.25	-1.2 ± 0.3	0.62	0.52 ± 0.02^{m}	-1.2	26.73 ± 0.01	$\cdots$	-285.9 ± 0.4	$\cdots$
Ross 451	M0	3800 ± 25^g	4.73 ± 0.01	-0.96 ± 0.02	0.5	0.31 ± 0.02^g	-0.96	24.74 ± 0.01	$\cdots$	-154.3 ± 0.3	$\cdots$
Ross 1044	M0	3754 ± 95^h	4.99 ± 0.2	-1.01 ± 0.21	0.3	0.38 ± 0.03^h	-1.01	26.71 ± 0.02	$\cdots$	-168.6 ± 0.3	$> 10^{ah}$
Kapteyn's Star	M1	3650 ± 80^i	4.96 ± 0.13	-0.5 ± 0.3	0.28	0.28 ± 0.01^p	-0.5	3.93 ± 0.01	$-4.2 - 9.15^{o,r}$	245.1 ± 0.1	$11.5^{+0.5}_{-1.5}\ (ai)$
GJ 411	M2	3530 ± 100^j	4.5 ± 0.01	-0.2 ± 0.1	0.44	0.41 ± 0.03^g	-0.2	2.55 ± 0.01	$-3.25 - 6.5^{o,s}$	-85.1 ± 0.1	$> 5^{ag}$
L 802-6	M3	3384 ± 61^k	5.08 ± 0.1	-0.47 ± 0.1	0.4	0.25 ± 0.11^{m}	-0.47	11.50 ± 0.01	1.70 ± 0.38^t	101.4 ± 0.4	3.04 ± 3.09^{aj}
Barnard's Star	M4	3332 ± 50^l	5.13 ± 0.01	-0.29 ± 0.2	0.23	0.187 ± 0.01^q	-0.29	1.83 ± 0.01	3.1 ± 1.2^u	-110.5 ± 0.1	$7 - 10^{ak}$

NOTE—For each star, the $T_{\rm eff}$, $\log(g)$, and [Fe/H] were obtained from a single reference and validated against visible/infrared photometry from the Vizier Photometric Viewer[a]. All distance and RV measurements are from Gaia Collaboration et al. (2021) and estimated masses from M. J. Pecaut & E. E. Mamajek (2013). Uncertainties on $T_{\rm eff}$, $\log(g)$, and [Fe/H] were estimated from inter-quartiles of values listed on simbad.u-strasbg.fr if the listed reference did not provide them.

References— (a) R. E. Luck (2017); (b) T. Bensby et al. (2014); (c) M. N. Perrin (1975); (d) J. A. Valenti & D. A. Fischer (2005); (e) K. G. Stassun et al. (2018); (f) This Work; (g) A. Y. Kesseli et al. (2019); (h) E. R. Newton et al. (2015); (i) G. Anglada-Escude et al. (2014); (j) S. Lépine et al. (2013); (k) E. Gaidos et al. (2014); (l) L. J. Rosenthal et al. (2021); (m) Gaia Collaboration et al. (2021); (n) N. Zacharias et al. (2012); (o) R. Glebocki & P. Gnacinski (2005); (p) A. Youngblood et al. (2022); (q) S. Peacock et al. (2022); (r) E. R. Houdebine (2010); (s) H. Jönsson et al. (2020); (t) P. B. Das et al. (2025); (u) P. Fouqué et al. (2018); (y) S. A. Stanford-Moore et al. (2020); (ac) H. Isaacson & D. Fischer (2010); (ad) H. Isaacson & D. Fischer (2010); (ae) H. Reggiani & J. Meléndez (2018); (af) C. K. Harada et al. (2024); (ag) J. Gagné & J. K. Faherty (2018); (ah) A. C. Schneider et al. (2019); (ai) E. Wylie-de Boer et al. (2010); (aj) J. Maldonado et al. (2020); (ak) I. Ribas et al. (2018)
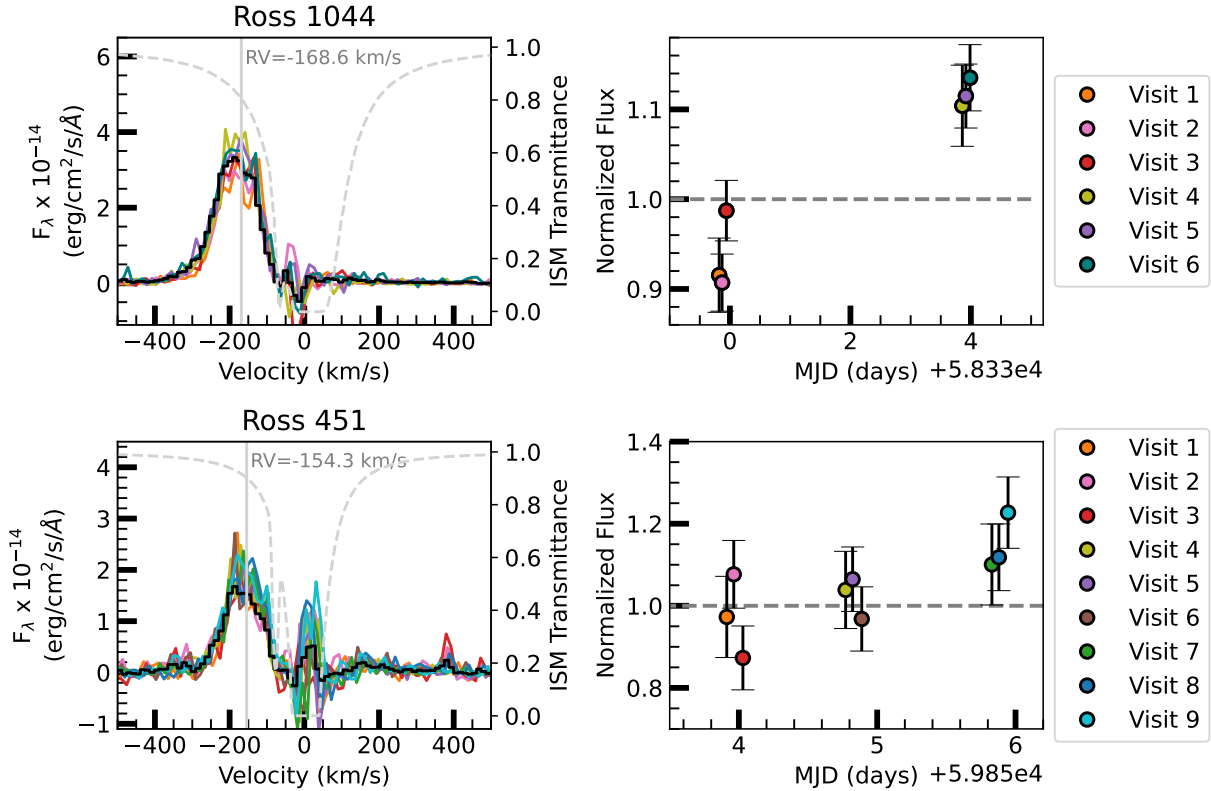
Figure 2. Of the 12 high RV stars with Lyα measurements, two have observations taken over multiple days and both exhibit variability on the order of 20% over the 3-4 day observing windows. *Left*: HST/STIS Lyα spectra of Ross 1044 (top) and Ross 451 (bottom) over multiple visits (various colors) compared to the final coadded spectrum in black. The ISM transmittance curves are plotted as gray dashed lines. *Right*: Lyα flux variability of Ross 1044 (top, adapted from A. C. Schneider et al. 2019) and Ross 451 (bottom), as measured over the observed spectrum from ±0.5 Å from the line center. Each set of points are normalized to the flux of the final coadded spectrum.

chromosphere, where previous downturns occurred, enhances the flux in the Lyα core without affecting the Lyman continuum.

Building on this, for the present study, from each star's 72-model grid, we identified chromospheric structures that fit the uncontaminated wings of the observed Lyα profiles within a reduced chi-squared threshold of $\Delta\chi^2_\nu \leq 4$ from the minimum (corresponding to 1σ uncertainty, given four three parameters). From these new subsets of models, we then generated updated grids by varying the minimum n=2 level population of H I at the chromosphere-transition region boundary, ranging from 0.3 to the maximum value in the chromosphere (typically $\sim$3) in steps of 0.1. As a result, the new grids contain sets of Lyα profiles with similar line widths but varying reversal depths[8].

We again applied the radial velocity shifts, multiplied by the appropriate ISM transmittance curves, and convolved the model spectra to the observational resolution. This time, instead of selecting models based solely on the uncontaminated wings, we identified the model with a χ^2_ν value closest to 1 across the full line width. We present these best-fitting models in Figure 1, where both the intrinsic model profiles and those modified by ISM transmittance are plotted against the observations (Appendix Figures 9, 10, and 11 show the adjustments made to the minimum n=2 level population of H I at the chromosphere-transition region boundary). The intrinsic profiles confirm moderate-to-no central reversals in K and M stars, with the deepest reversal appearing in the hottest star in our sample ($\sim$5500 K) and no reversal in the coolest ($\sim$3300 K). We analyze trends with these intrinsic Lyα profiles in Section 4.

---

[8] Similar to findings in S. Peacock et al. (2022), adjusting this minimum has negligible effect on the rest of the computed spectrum, with the flux across EUV wavelengths (100 – 912 Å) and the Hα line changing by $< 1\%$. This lack of change does not imply that Lyα should not correlate with either, but rather that they are less sensitive to changes in the $n = 2$ population of H I in these layers.
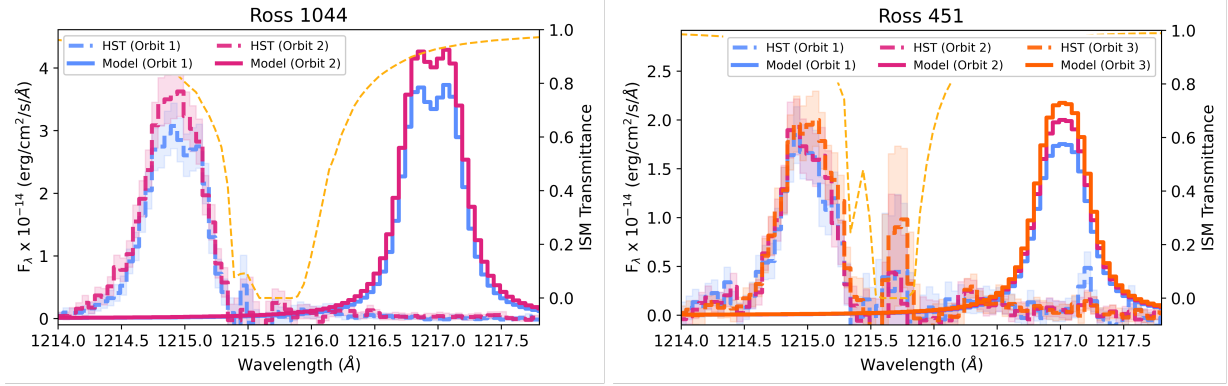
Figure 3. Measured (dashed) and modeled (solid; and shifted in wavelength for visual clarity) Lyα profiles for Ross 1044 (*left*) and Ross 451 (*right*) from the multiple HST orbits that exhibited variable behavior. The modeled profiles show the stellar emission in the absence of ISM absorption. For Ross 1044, there is a 5% difference in self-reversal depth as measured via peak-to-trough ratio; there is no difference in peak-to-trough ratio for Ross 451. The ISM transmittance curve is plotted as the yellow dashed line.

3.1. *Variable Stars*

For most stars, Lyα variability can originate from three primary sources: 1) intrinsic stellar processes (e.g., rotation or magnetic activity), 2) escaping hydrogen from a transiting planet undergoing mass-loss, and 3) instrumental effects. For HST/STIS, there exists a breathing effect caused by thermal cycling as the spacecraft moves between orbital day and night that can introduce small flux variations within (<10%) and between (1–3%) orbits (R. A. Kimble et al. 1998; T. M. Brown et al. 2001; L. Ben-Jaffel 2007; D. Ehrenreich et al. 2012; W. C. Waalkes et al. 2019). For the $52'' \times 0''.1$ slit aperture used in the present observations, the photometric repeatability is approximately 8.8% root mean square (RMS), consistent with expectations for smaller STIS apertures subject to thermal breathing effects (R. Bohlin & G. Hartig 1998).

In the Sun, Lyα flux varies by 1-30% during minutes-long flares (R. O. Milligan et al. 2020; H. J. Greatorex et al. 2023), 25–40% over the 27-day solar rotation cycle and by 80–155% over its 11-year solar cycle (L. Bossy & M. Nicolet 1981; J. L. Lean & T. P. Repoff 1987). The core of the line shows the most variability, the wings of the profile remain relatively stable. At solar maximum, the increased emission partially fills in the self-reversal, leading to a lower peak-to-trough ratio (e.g., W. Curdt & H. Tian 2010; I. Kowalska-Leszczynska et al. 2018; S. Gunár et al. 2020).

In low-mass stars, which are typically more active than solar-type stars, similar variability has been observed in other UV spectral lines (e.g., R. O. P. Loyd & K. France 2014; G. M. Duvvuri et al. 2023), with measured variability ranging from 1% to 41% over short timescales (minutes to hours). Short-term variations are caused by flares, fluctuations and stochastic variability, intermediate-term variations (weeks to months) result from stellar rotation, active region evolution, and episodes of major activity, while long-term variations (years) arise from stellar cycles and the evolution of active regions.

A common characteristic of high-RV stars is that they are typically old (Table 2), having had sufficient time for dynamical interactions within the Galaxy to increase their motion and shift them to high radial velocities (e.g., R. Wielen 1977; B. Nordström et al. 2004). Older stars generally exhibit lower levels of UV activity than their younger counterparts; however, M and K dwarfs are still capable of regular flare activity, even in seemingly "inactive" stars (R. O. P. Loyd et al. 2018; K. France et al. 2020). While R. O. P. Loyd et al. 2018 found that Lyα typically shows little response to flares in low-mass stars, those observations lacked information on the line core.

In contrast, we find evidence of detectable Lyα variability in two old, high-RV stars on timescales that could be related to flare activity or stellar modulation (Figure 2). Specifically, we detect Lyα variability in one of our new targets, Ross 451, an M0V star. A. C. Schneider et al. 2019 previously reported similar variability in the other M0V star in this sample, Ross 1044. Both stars exhibit ≈20% flux variations across multiple visits, primarily in the core of the emission line. As these variations are much larger than the 8.8% flux changes associated with STIS thermal breathing for this aperture size (R. Bohlin & G. Hartig 1998), and are confined to the line core rather than producing wavelength-independent fluctuations across the entire profile, we interpret them as likely intrinsic to the star rather than instrumental in origin. Among the 12 high-RV stars with Lyα measurements, these are the only two observed

Table 3. Lyα Line Properties

Star	% of line exposed	Peak-to-trough Ratio	log N(H I) (cm^{-2})	$F_{Ly\alpha,surface}$ (erg cm^{-2} s^{-1})	$F_{Ly\alpha,HZ}$ (erg cm^{-2} s^{-1})
HD 64090	83%	1.88	$18.46^{+0.15}_{-0.17}$	$2.24 \pm 0.07 \times10^5$	5.80 ± 1.75
HD 134439	89%	1.21	$18.83^{+0.09}_{-0.11}$	$2.51 \pm 0.07 \times10^5$	8.74 ± 2.57
HD 134440	88%	1.28	$18.51^{+0.26}_{-0.46}$	$1.48 \pm 0.07 \times10^5$	5.80 ± 1.68
HD 191408	49%	1.28	18.28 ± 0.02^a	$2.88 \pm 0.05 \times10^5$	12.14 ± 3.50
Ross 825	69%	1.14	18.80^b	$4.90 \pm 0.21 \times10^4$	2.25 ± 0.64
HIP 117795	92%	1.14	$18.13^{+0.53}_{-0.42}$	$2.40 \pm 0.08 \times10^5$	17.88 ± 4.87
Ross 451	84%	1.00	$18.41^{+0.28}_{-0.48}$	$3.24 \pm 0.51 \times10^4$	3.22 ± 0.85
Ross 1044	85%	1.00	18.86^b	$7.94 \pm 0.08 \times10^4$	8.27 ± 2.19
Kapteyn's Star	95%	1.10	$17.98^{+0.36a}_{-0.32}$	$1.05 \pm 0.05 \times10^5$	12.14 ± 3.18
GJ 411	60%	1.02	17.84 ± 0.03^a	$7.24 \pm 0.06 \times10^4$	9.55 ± 2.48
L 802-6	47%	1.00	$18.39^{+0.25}_{-0.33}$	$2.75 \pm 0.17 \times10^4$	4.28 ± 1.10
Barnard's Star	64%	1.00	17.72 ± 0.03^a	$3.62 \pm 0.04 \times10^4$	5.99 ± 1.53

NOTE—Fraction of Lyα flux exposed is calculated as $\frac{(intrinsic\ model \times ISM)}{intrinsic\ model}$. Lyα fluxes are derived from the intrinsic models by integrating over ± 0.75 Å from line center, with uncertainties propagated from the observational values. Habitable zone fluxes are computed following R. K. Kopparapu et al. (2014), assuming a 1 Earth-mass planet located at the midpoint between the Recent Venus and Early Mars limits.

References—(a) A. Youngblood et al. 2022 ; (b) A. C. Schneider et al. 2019

over several days, and both display similar behavior on comparable timescales. The other stars with multiple orbits had their observations occur on a single day within a < 3 hour period (excluding the failed visit of HIP 117795 on Oct 14).

When modeling the observations for these two stars individually by orbit (coadding the 3 visits per orbit), we find that for Ross 451, the line strength varies between orbits; however, each observation is best fit by a line profile without self-reversal, with a consistent peak-to-trough ratio of 1 across all three orbits. In contrast, for Ross 1044, the two observed orbits are best fit by different models, each yielding slightly different peak-to-trough ratios of 1.06 and 1.11 (Figure 3). This behavior is reminiscent of the solar Lyman-alpha profile, which also exhibits variations in self-reversal depth and peak-to-trough ratio over the solar cycle due to changes in chromospheric activity. The observed variability in Ross 1044 suggests that localized enhancements in chromospheric emission, such as flares or active regions, may temporarily reduce the depth of the self-reversal. Additionally, rotational modulation could contribute, as active regions or plage rotating in and out of view may alter the observed profile over time, similar to how solar Lyman-alpha emission varies with the passage of active regions across the solar disk.

Ross 451 and Ross 1044 are both M0 dwarfs with similar radial velocities (–168.6 and –154.3 km/s), and both show comparable levels of Lyα variability. While the alignment in velocity and variability might suggest a common cause, it appears to be a coincidence. In principle, variability could be due to ISM effects or instrumental limitations (e.g., the use of a narrow 0″.1 slit). However, given that both stars are largely clear of the ISM (the transmittance at the line core is ≈80%) and that the structure of an intervening ISM cloud is unlikely to vary on timescales of a few days, the observed changes are unlikely to be caused by ISM variability. Instrumental effects, such as potential slit losses associated with the narrow 0″.1 aperture, cannot be entirely ruled out, but the variability is strongly wavelength-dependent: when the flux is computed in 0.1 Å bins across the line profile, the variability ranges from ≈10% to 60%. This wavelength dependence, combined with the temporal behavior, points to an origin intrinsic to the star. A. C. Schneider et al. (2019) previously suggested that the Lyα variability in Ross 1044 may arise from rotational modulation or stellar flares, an interpretation that aligns with our results.

4. ANALYSIS

T. R. Ayres (1979), J. L. Linsky (1980), A. Youngblood et al. (2022) and A. Taylor et al. (2024) have connected chromospheric emission line properties as a function of chromospheric heating, $T_{\rm eff}$, surface gravity, and elemental abundance. With the intrinsic profiles presented in this paper, we assess whether surface Lyα line flux and the self-reversal depth (quantified as the peak-to-trough ratio) are also connected.

4.1. *Connections Between Lyα Flux and Stellar Parameters*

In Figure 4, we examine trends in Lyα profile properties (Table 3) as functions of $T_{\rm eff}$ and surface gravity. While instrumental broadening can reduce the measured peak-to-trough ratio, our calculations are based on intrinsic models treated consistently, ensuring that trend identification remains unaffected. However, we note that the method for quantifying the Sun's values, taken from A. Youngblood et al. (2022), differ from the rest of our sample and are included for context rather than in the linear regression fits.

We find strong correlations (R > 0.7, $p < 0.01$) between both Lyα surface flux and peak-to-trough ratio with $T_{\rm eff}$, indicating that hotter stars emit more Lyα surface flux. A 5500 K star emits approximately ten times more Lyα flux at its surface than a 3500 K star. Consistent with previous studies, we observe deeper self-reversal in earlier spectral types, with all K stars exhibiting some degree of reversal, whereas four of the six M stars suggest no self-reversal, and the other two only slight.

There is overlap between three M stars analyzed in A. Youngblood et al. (2022) and those in our sample: Kapteyn's Star, GJ 411, and Barnard's Star. A. Youngblood et al. (2022) used reconstruction methods that tend to favor very slight reversal depths for M stars (shown in Appendix Figure 11), reporting peak-to-trough ratios of 1.11 ± 0.04 for Kapteyn's Star, $1.10^{+0.05}_{-0.04}$ for GJ 411, and 1.03 ± 0.02 for Barnard's Star. In our analysis, we examine six M stars in total. Of the three M stars not in A. Youngblood et al. (2022), none exhibit self-reversals. For the three overlapping stars, we find no reversal in Barnard's Star (1.0), a slightly smaller reversal in GJ 411 (1.03), and the same value for Kapteyn's Star (1.11). These results further reinforce the trend that self-reversal is minimal or absent in M stars, with only slight variations depending on the reconstruction method used.

In line with the influence of reconstruction method choices and the limitations of small-number statistics, A. Young-blood et al. (2022) found a clear correlation between peak-to-trough ratio and log(g), with lower log(g) corresponding to deeper self-reversal. We see a similar trend, though with a weaker linear regression fit. Our larger sample (12 stars vs. 5, or 13 vs. 6 including the Sun) contributes to this difference, along with discrepancies such as A. Youngblood et al. (2022) finding a stronger reversal depth for HD 191408 and including 82 Eri (G8V), which we excluded due to spectral type.

4.2. *Identifying Trends with Atmospheric Structure*

The stark difference in self-reversal depths between K and M stars suggests a fundamental shift in the structure and dynamics of their upper atmospheres. This may be linked to differences in chromospheric activity, turbulence, or radiative transfer effects. To investigate this further, we examine trends in the model chromospheric structures that best reproduce the observed Lyα profiles. Figure 5 shows the temperature-column mass structures for the 12 stars, with shaded regions highlighting the approximate temperature ranges where the wings and core of Lyα forms. A clear pattern emerges: in K stars, the chromosphere tends to start deeper in the atmosphere, at column masses around $10^{-4.5}$ to 10^{-4} cm s^{-1}, and extends over a larger range (Δcmass $= 10^{1.5}$ cm s^{-1}). M stars, on the other hand, have more compressed chromospheres that initiate at lower column masses, between column masses of $10^{-5.5}$ to 10^{-5} cm s^{-1}, with thicknesses of Δcmass $= 10^{1}$ - $10^{1.5}$ cm s^{-1}. Ross 825 stands out as an outlier, preferring a much broader chromosphere (Δcmass $=10^{3.5}$ cm s^{-1}) that begins at 10^{-3} cm s^{-1}.

In the present work, we focus exclusively on fitting Lyα to maintain consistency across the sample and to identify general trends. It is important to note that since these models are constrained by a single spectral feature (the Lyα line), they may not fully represent the broader UV spectrum. For example, Ross 825, Ross 1044, and Kapteyn's Star were previously modeled in S. Peacock et al. (2022) using both NUV and Lyα flux, resulting in notably different chromospheric structures. The chromospheric structure of Ross 825, which stands out as an outlier in the present Lyα-only fits, illustrates the impact of including NUV constraints. As shown in S. Peacock et al. (2022), when GALEX NUV photometry is simultaneously fit alongside Lyα, the resulting model prefers a more compressed chromosphere, initiating at higher column mass ($10^{-5.5}$ to $10^{-3.5}$ g cm^{-2}) and aligning more closely with the other K stars in the sample. In contrast, Ross 1044 requires a significantly wider chromosphere when both Lyα and NUV are fit, with the
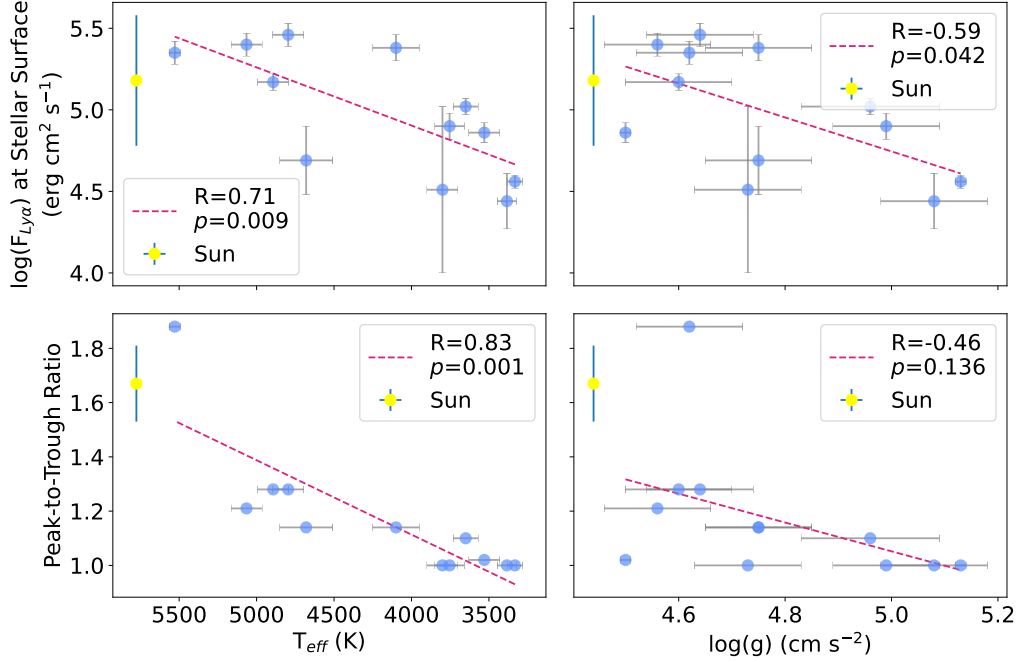
Figure 4. The logarithm of Lyα flux ($\log(F_{Ly\alpha})$) at the stellar surface (*top row*) and peak-to-trough ratio of the intrinsic Lyα profile (*bottom row*) versus T_{eff} (*left column*) and the logarithm of surface gravity (*right column*). Linear regression fits are plotted as pink dashed lines and the Sun is plotted as a yellow circle (the Sun is excluded from the fits). We find strong trends ($R > 0.7$, $p < 0.01$) between T_{eff} and both $\log(F_{Ly\alpha})$ and peak-to-trough ratio. We note that the K0 star HD 64090 (5528 K) exhibits a markedly deeper self-reversal than the rest of the sample, including the Sun, and appears as an outlier in the peak-to-trough ratio plots. This pronounced reversal is likely attributable to the star's old age and correspondingly low activity level, consistent with the behavior observed in the Sun, whose core reversal deepens during periods of low activity and becomes more filled in when activity is higher.

chromospheric temperature rise beginning as deep as 10^{-2} g cm^{-2} and extending up to $10^{-6.5}$ g cm^{-2}, suggesting an extended heating region. Kapteyn's Star also shows a systematic shift: when NUV data are included, the entire chromosphere is shifted uniformly to lower column masses by Δcmass $= 10^{0.5}$ g cm^{-2}, a trend consistent with the general behavior identified in this present study. These comparisons reinforce that while the Lyα-only models capture key aspects of the upper atmospheric structure, simultaneous fits including NUV fluxes can shift or reshape the inferred chromospheres in systematic ways.

To assess the level of consistency between our Lyα-only models and available NUV measurements, we spot-checked these same three stars by computing synthetic NUV fluxes from our best-fit models and comparing them to the observed values. The results show general agreement within a factor of a few: for Ross 825, the observed GALEX NUV flux is $(1.37 \pm 0.12) \times 10^{-12}$ erg s^{-1} cm^{-2}, compared to a model flux of 1.80×10^{-12} erg s^{-1} cm^{-2}; for Kapteyn's Star, the observed value is $(1.09 \pm 0.01) \times 10^{-12}$ erg s^{-1} cm^{-2} and the model predicts 2.94×10^{-12} erg s^{-1} cm^{-2}; and for Ross 1044, the observed flux is $(1.47 \pm 0.46) \times 10^{-13}$ erg s^{-1} cm^{-2} while the model yields 1.39×10^{-13} erg s^{-1} cm^{-2}. These comparisons suggest that our models constrained by Lyα alone are broadly consistent with the available NUV data, despite not explicitly fitting to it.

The difference in chromospheric structures between K and M stars directly impacts the Lyα flux. Although M star chromospheres are more compressed in column mass, they can still exhibit strong chromospheric emission because this compression leads to locally higher gas densities. This may seem counterintuitive, since their chromospheres begin at lower column masses than those of K stars. However, the key lies in the atmospheric structure: M dwarfs have smaller pressure scale heights, so a given change in column mass corresponds to a smaller change in geometrical height. As a result, material at a given column mass is located deeper in the atmosphere (at higher gas pressure and density) in M stars than in K stars. Thus, even though M dwarf chromospheres span a narrower range in column mass, the local densities in these layers can be higher, enhancing their chromospheric emission. Nevertheless, K stars tend to have deeper chromospheres overall, which leads to systematically higher Lyα surface fluxes compared to M stars.
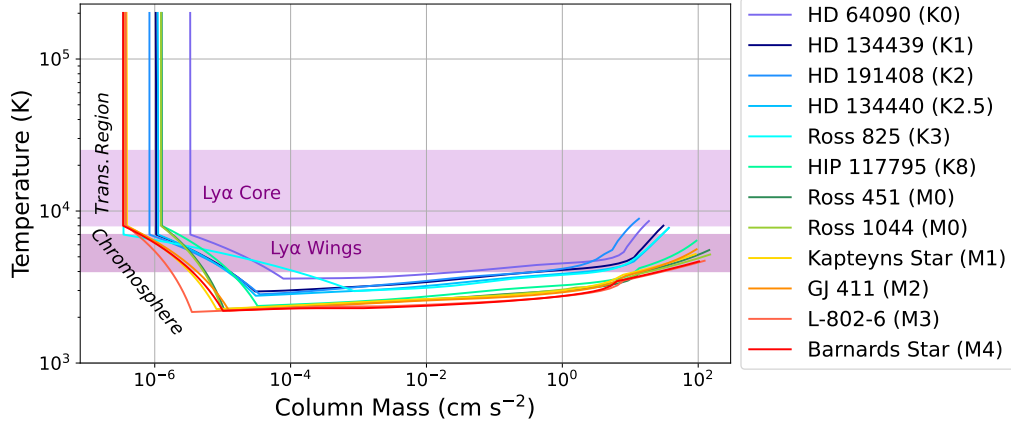
Figure 5. Temperature-column mass structures for the models of each star. We shade the approximate temperature ranges over which the core and wings of Lyα forms in purple (≈8000–25,000 K for the core, and ≈4000–7500 K for the wings), the actual range of temperatures varies by star and is determined by where the optical depth, $\tau(\lambda)$, equals to one.

The transition region's temperature gradient is extremely steep (so much so that it's hard to distinguish in the plot) but no obvious trends emerge, with values spanning $\nabla T_{TR} = 10^{7.5}\text{-}10^9$ g^{-1} cm^2. One key difference between K and M stars is the onset temperature of the transition region: around 7000 K for K stars and 8000 K for M stars. This is set by the point where hydrogen becomes fully ionized, triggering thermal instability in the transition region. This is the same part of the atmosphere where we imposed minimum values for n$_{NLTE}$ /n$_{LTE}$ in the n=2 state of H I in order to reproduce the observations, specifically the flux in the Lyα core.

Figure 6 compares these imposed minimum values with $T_{\rm eff}$ and $\log(g)$. We find weak correlations (R=0.49, 0.26; p=0.1, 0.41) between the minimum n$_{NLTE}$ /n$_{LTE}$ at the transition region-chromosphere boundary and these parameters. However, when considering the ratio of the minimum value to the corresponding maximum n$_{NLTE}$ /n$_{LTE}$ in the chromosphere, the correlation with $T_{\rm eff}$ strengthens significantly (R=0.75, p=0.01). This result provides a key step toward improving stellar modeling. The strong correlation between the ratio of minimum to maximum n$_{NLTE}$ /n$_{LTE}$ and $T_{\rm eff}$ suggests that we can apply a systematic correction to model departures from LTE. By incorporating this relationship, we can better constrain the excitation state of hydrogen in the chromosphere and transition region, leading to more accurate predictions of Lyα emission across different stellar types.

4.3. *Identifying Trends with Flux at the Habitable Zone*

In Figure 4, we find that earlier spectral types emit more Lyα flux at the stellar surface. This suggests that planets at the same orbital distance around K stars likely experience stronger Lyα-driven atmospheric photodissociation than those around M stars. We note that this trend is driven primarily by the larger radii of K stars, rather than implying that K stars are intrinsically more active than M stars. However, when scaling the Lyα flux to the habitable zone (HZ) distance (R. K. Kopparapu et al. 2014), the Lyα flux is comparable for both K and M stars, ranging from ∼2 to 20 erg cm^{-2} s^{-1} (Table 3). This is consistent with the findings of T. Richey-Yowell et al. (2023), who reported that total UV fluxes in the HZs of K and M dwarfs are broadly similar, despite differences in stellar size and surface flux.

Figure 7 illustrates the comparatively direct Lyα measurements from this study alongside reconstructed fluxes from previous works (B. E. Wood et al. 2005; J. L. Linsky et al. 2014; V. Bourrier et al. 2017a,b; K. Melbourne et al. 2020; A. Youngblood et al. 2022; A. Sandoval et al. 2023), plotted against $T_{\rm eff}$ at the HZ. Since our sample is likely old (based on kinematics), we highlight stars older than 1 Gyr in color, while younger ones are shown in gray for comparison.

For the full sample of stars older than 1 Gyr, a planet in the HZ receives increasing Lyα flux with decreasing $T_{\rm eff}$. A linear regression fit to the data suggests that a planet in the HZ of a 3000 K star receives ≈2.5× more Lyα flux than a planet in the HZ of a 6000 K star. However, when isolating the high RV stars, which are likely older than 5 Gyr, the trend flattens. In contrast, among young stars (<1 Gyr), the Lyα flux around later-type stars is even higher relative to earlier types, a 3000 K star emits ≈10× more Lyα flux than a 6000 K star, emphasizing the role of stellar age. Notably, the high RV stars from this study, A. Youngblood et al. (2022), and the Sun align along the same linear regression, suggesting that older stellar populations may follow a common evolutionary trajectory in their HZ Lyα flux. This alignment also reinforces the reliability of the comparatively direct measurements used in this work.
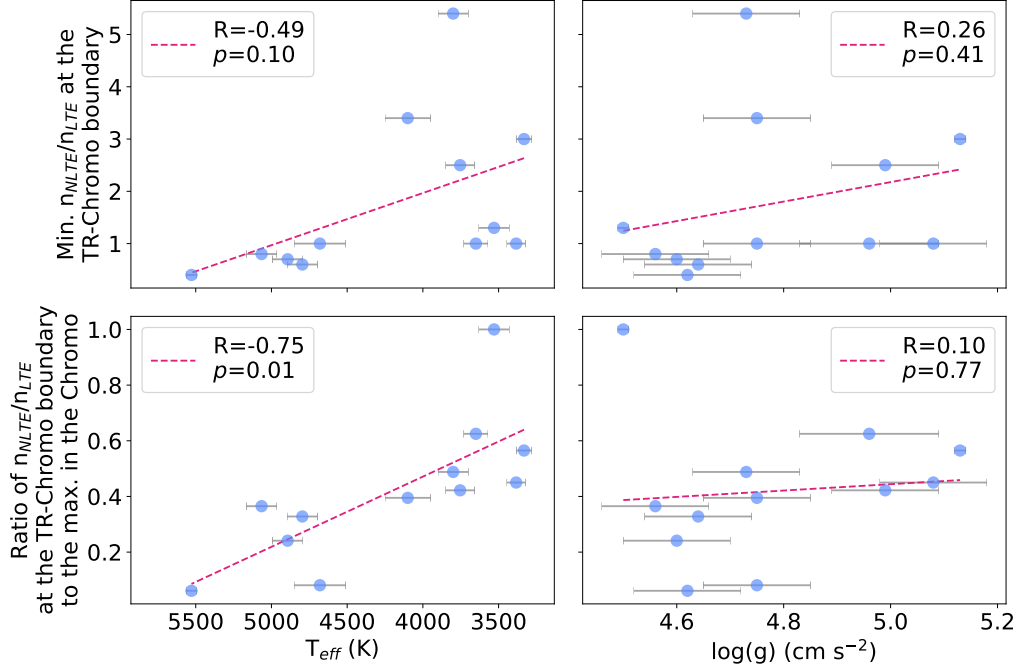
Figure 6. Minimum values for n_{NLTE}/n_{LTE} in the n=2 state of H I at the transition region-chromosphere boundary (*left column*) and the ratio of that value to the corresponding maximum n_{NLTE}/n_{LTE} in the chromosphere (*right column*) versus $T_{\rm eff}$ (*left column*) and the logarithm of surface gravity (*right column*). Linear regression fits are plotted as pink dashed lines. We find a strong trend (R = 0.75, p=0.01) between $T_{\rm eff}$ and the ratio of the minimum n_{NLTE}/n_{LTE} at the transition region-chromosphere boundary to the corresponding maximum value in the chromosphere.

Reconstructed Lyα fluxes are widely used to correlate with spectral lines, UV photometry, and X-ray fluxes, aiding habitability assessments across stellar types. However, assumptions in Lyα reconstructions, particularly regarding the shape of the intrinsic line profile, may introduce systematic offsets. A. Sandoval et al. (2023) revised earlier reconstructions from A. Youngblood et al. (2016), following updated methodology from A. Youngblood et al. (2022) with improved parameterizations of both the intrinsic line wings and the central reversal feature. Their analysis revealed that for M dwarfs, previous flux estimates were overestimated by 10–35%, while for K stars (whose Lyα lines exhibit deeper central reversals) the overestimates were more severe, by factors of 3–5. This disparity underscores the importance of including accurate reversal structures, especially for earlier-type stars.

Given this, it is possible that all reconstructed Lyα fluxes may be systematically overestimated to some degree, depending on how the intrinsic line profile was treated. While many of the hotter stars in Figure 7 already include a reversal in their reconstructions, if their fluxes are still too high, this could reflect underlying issues such as incorrect assumptions about the ISM H I column density, which strongly affects the inferred flux. However, stellar age also plays a critical role, as older stars may truly emit less Lyα flux, so distinguishing between reconstruction error and intrinsic stellar evolution remains an important challenge.

If dwarf stars emit less intrinsic Lyα radiation than previously thought, the radiation environments of their exoplanets may need to be revisited. However, in S. Peacock et al. (2022), we explored the impact of varying Lyα fluxes by factors of 0.35 to 1.5 on the photochemistry of high molecular weight terrestrial exoplanet atmospheres. We found that these changes produced only minor variations in spectrally active gases, and the resulting differences in atmospheric spectra would be undetectable with current observatories like JWST. This suggests that, at least for terrestrial planet atmospheres, moderate uncertainties in Lyα flux are unlikely to significantly affect the interpretation of transmission spectra. While continued refinement of reconstruction techniques remains valuable, especially for broader stellar and planetary applications, the near-term implications for atmospheric modeling appear to be limited in scope.

4.4. *The Role of Stellar Age in Shaping Lyα Emission*

Several studies have investigated how Lyα emission evolves with stellar age, with implications for planetary atmospheric evolution and habitability. For instance, C. P. Johnstone et al. (2021) model the decay of X-ray, EUV, and
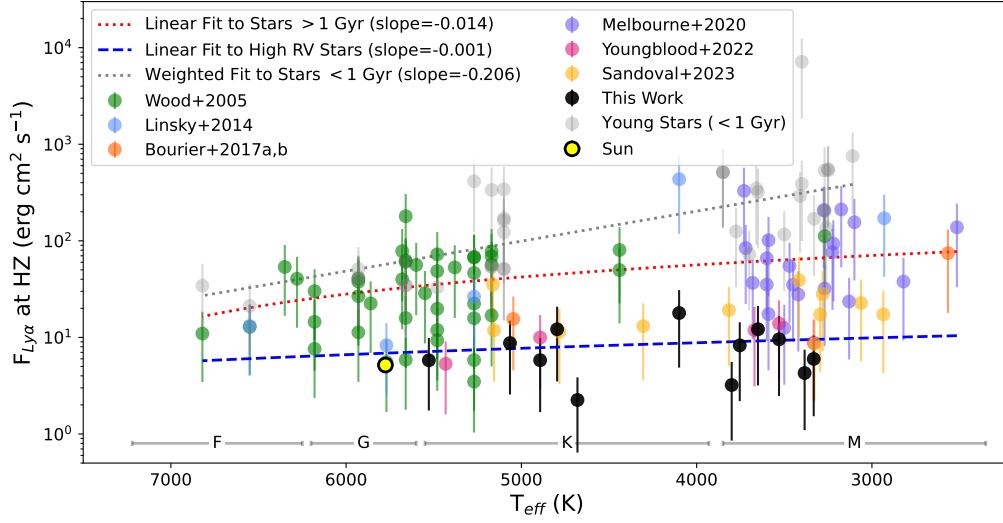
Figure 7. Reconstructed (B. E. Wood et al. 2005; J. L. Linsky et al. 2014; V. Bourrier et al. 2017a,b; K. Melbourne et al. 2020; A. Sandoval et al. 2023) and directly observed (This work, A. Youngblood et al. 2022) Lyα fluxes scaled to the habitable zone, following R. K. Kopparapu et al. (2014) and assuming a 1 Earth-mass planet. Error bars give the flux range between the Recent Venus and Early Mars limits, not the estimated uncertainties. All stars older than 1 Gyr are plotted in color, and those younger than 1 Gyr in gray. Linear regression fits to all stars >1 Gyr (*red dotted line*), to just the high RV stars from this work and A. Youngblood et al. 2022 (*blue dashed line*), and a weighted fit to the young stars (<1 Gyr; *gray dotted line*) are shown. We note that the Sun and the A. Sandoval et al. 2023 values (improved Lyα reconstructions from those presented in A. Youngblood et al. 2016) align more closely with the high RV fit line.

378 Lyα emission over time, finding that Lyα decays more slowly than both X-ray and EUV luminosities. This leads to
379 increasing $F_{\mathrm{Ly}\alpha}/F_{\mathrm{X}}$ and $F_{\mathrm{Ly}\alpha}/F_{\mathrm{EUV}}$ ratios with age, particularly beyond ~1 Gyr. S. G. Engle (2024) extend this
380 picture observationally for M dwarfs, showing a saturation phase lasting ~720 Myr for early-M dwarfs and ~1.5 Gyr
381 for mid-to-late Ms, though both phases are poorly constrained due to sparse data. Notably, S. G. Engle (2024) find
382 that Lyα luminosity relative to bolometric luminosity is systematically higher in cooler, later-type M dwarfs, consistent
383 with the trends reported by J. L. Linsky et al. (2020).

384 Our results complement these studies by providing comparatively direct Lyα observations for a set of 12 K and M
385 dwarfs, with age estimates available for 10 of them. While our sample size is too small to resolve saturation-phase
386 durations or perform subtype-separated fits, we observe general agreement with the evolutionary patterns described
387 above. Among stars older than 1 Gyr, the Lyα flux at the HZ decreases with increasing T_{eff}, suggesting that lower-mass
388 stars remain relatively Lyα-active for longer. Moreover, our subset of high radial velocity stars (likely all older than 5
389 Gyr) lies along a tight Lyα–T_{eff} relation, consistent with an evolved population that may follow a common decay track.
390 These findings echo the late-time convergence seen in C. P. Johnstone et al. (2021) and reinforce the interpretation
391 that Lyα emission persists as a significant UV source even in old, low-mass stars.

392 To further investigate age evolution, we compared our observationally constrained $L_{\mathrm{Ly}\alpha}/L_{\mathrm{bol}}$ ratios to the empirical
393 relations from S. G. Engle (2024) for M dwarfs (Figure 8). Our three M0–M2 stars fall within or exceeding the upper
394 edge of the model's 1σ envelope at ages > 5 Gyr, with a possible trend of increasing $L_{\mathrm{Ly}\alpha}/L_{\mathrm{bol}}$ with age across these
395 objects. In contrast, our two mid-M stars (L 802-6 and Barnard's Star) lie significantly below the empirical M2.5–M6.5
396 relation, even after accounting for model uncertainties. This trend is in tension with the conclusions of S. G. Engle
397 (2024) and J. L. Linsky et al. (2020), who find that $L_{\mathrm{Ly}\alpha}/L_{\mathrm{bol}}$ increases toward cooler, later-type M dwarfs. Our data
398 suggest instead that, at least among older field stars, early-M dwarfs may retain stronger relative Lyα emission than
399 their mid-M counterparts. This discrepancy could reflect intrinsic variability, sampling effects, or limitations in the
400 Lyα reconstructions at late ages.

5. CONCLUSIONS

402 We present Lyα profiles for 12 high radial velocity stars, with ≈50–95% of their intrinsic profiles directly observable.
403 This sample uniformly covers the critical K to M T_{eff} range, allowing us to identify the point where self-reversals in
404 Lyα profiles become significant ($T_{\mathrm{eff}} > 4000$ K) and to reduce systematic uncertainties in future profile reconstructions.
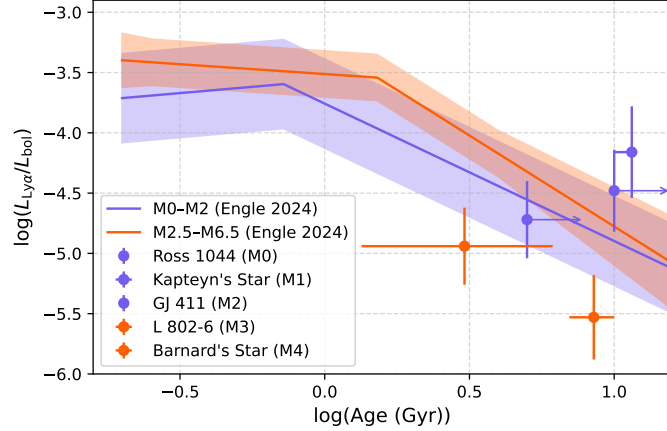
Figure 8. The evolution of $\log(L_{\mathrm{Ly}\alpha}/L_{\mathrm{bol}})$ as a function of stellar age for M dwarf stars. Solid lines show the parameterized empirical trends for M0–M2 and M2.5–M6.5 spectral types from S. G. Engle (2024), with shaded regions representing 1σ uncertainties on the fits. Overplotted are our sample stars, color-coded by spectral type: M0–M2 (purple) and M3–M4 (orange). The three M0–M2 stars lie within or exceeding the upper bound of the extrapolated uncertainty envelope at older ages. In contrast, the M3–M4 stars fall significantly below the empirical track, suggesting either lower intrinsic activity or potential limitations of the model extrapolation at late ages for mid-M dwarfs.

We find that Lyα reversal depth correlates with T_{eff}—as T_{eff} decreases, self-reversals become less pronounced, with M stars exhibiting little to no reversal.

Two stars, Ross 1044 and Ross 451, were observed over multiple days, revealing $\sim$20% variability. For Ross 1044, the self-reversal depth fluctuated by 5% over a timescale of less than a week, whereas Ross 451, which lacks a reversal, showed no change in peak-to-trough ratio. In both cases, variability was localized to the line core, mirroring solar behavior. This suggests that Lyα variability in other systems may be underestimated when the core is fully absorbed—if only the wings are observable, they may appear stable while significant variations occur in the unseen core. Given that these two stars are old, this effect may be even more pronounced in younger, more active stars, similar to the Sun, which exhibits up to 155% variation over its 11-year cycle.

Beyond variability, we examined the relationship between Lyα flux, atmospheric structure, and stellar parameters. We find strong correlations between Lyα flux, peak-to-trough ratio, and the departure coefficient, n_{NLTE}/n_{LTE}, in the n=2 state of H I with T_{eff}. These trends provide critical constraints for refining stellar atmosphere models, particularly for K and M dwarfs, where direct measurements of intrinsic Lyα profiles remain difficult.

Comparing reconstructed Lyα flux in the HZ of typical stars and high radial velocity stars reveals a systematic offset: among stars older than 1 Gyr, the high-RV stars show consistently higher flux, with a mild trend indicating that M stars may have stronger HZ Lyα flux than G and K stars. However, for high radial velocity stars, the trend is flat. This offset may stem from differences in age, as high radial velocity stars are likely older (>5 Gyr), or from overestimated reconstructed fluxes. The latter is supported by the Sun's directly measured value and improved reconstructions of M and K stars from A. Sandoval et al. 2023, which align more closely with the high radial velocity sample.

Finally, we compared $L_{\mathrm{Ly}\alpha}/L_{\mathrm{bol}}$ for the M dwarfs in our sample to existing empirical estimates from S. G. Engle (2024). Our results suggest that early-M stars maintain higher relative Lyα emission at late ages than mid-M stars, contradicting the trend of increasing activity toward later spectral types reported in previous studies. Due to the scarcity of high radial velocity stars enabling intrinsic Lyα profile reconstruction, this dataset likely represents the most complete observational sample possible, emphasizing the importance of developing refined models to fully capture M dwarf chromospheric evolution.

Overall, this work provides key observational benchmarks for Lyα emission across K and M stars, reducing uncertainties in reconstructions and informing models of stellar atmospheres and exoplanet environments. Future observations of these stars, particularly to better quantify short- and long-term variability, will further refine our understanding of stellar UV radiation and its impact on exoplanet atmospheres and habitability.

16

APPENDIX

S. Peacock et al. (2022) found that the depth of the self-reversal in the Lyα line directly depends on the ratio of the non-local thermodynamic equilibrium (NLTE) to LTE number density (n_{NLTE}/n_{LTE}) for hydrogen in the n=2 state near the transition region-chromosphere boundary. Our initial model successfully reproduced the observed Lyα line widths but severely underestimated the line core due to a sharp decrease in this region. To match the full line profile, we imposed minima on the n=2 level population of H I at the chromosphere-transition region boundary. The following figures compare the initial and improved models, showing n_{NLTE}/n_{LTE} versus column mass and the computed Lyα profiles against observations.

Facilities: HST(STIS)

REFERENCES

Anglada-Escude, G., Arriagada, P., Tuomi, M., et al. 2014, VizieR Online Data Catalog, J/MNRAS/443/L89

Ayres, T. R. 1979, ApJ, 228, 509, doi: 10.1086/156873

Baron, E., & Hauschildt, P. H. 2007, A&A, 468, 255, doi: 10.1051/0004-6361:20066755

Ben-Jaffel, L. 2007, ApJL, 671, L61, doi: 10.1086/524706

Bensby, T., Feltzing, S., & Oey, M. S. 2014, A&A, 562, A71, doi: 10.1051/0004-6361/201322631

Bohlin, R., & Hartig, G. 1998,, STIS Instrument Science Report 98-20, 31 pages

Bossy, L., & Nicolet, M. 1981, Planet. Space Sci., 29, 907, doi: 10.1016/0032-0633(81)90080-5

Bourrier, V., Ehrenreich, D., Wheatley, P. J., et al. 2017a, A&A, 599, L3, doi: 10.1051/0004-6361/201630238

Bourrier, V., de Wit, J., Bolmont, E., et al. 2017b, AJ, 154, 121, doi: 10.3847/1538-3881/aa859c

Brown, T. M., Charbonneau, D., Gilliland, R. L., Noyes, R. W., & Burrows, A. 2001, ApJ, 552, 699, doi: 10.1086/320580

Cuntz, M., & Guinan, E. F. 2016, ApJ, 827, 79, doi: 10.3847/0004-637X/827/1/79

Curdt, W., & Tian, H. 2010, in Astronomical Society of the Pacific Conference Series, Vol. 428, SOHO-23: Understanding a Peculiar Solar Minimum, ed. S. R. Cranmer, J. T. Hoeksema, & J. L. Kohl, 81, doi: 10.48550/arXiv.1002.3551

Das, P. B., Zucker, D. B., De Silva, G. M., et al. 2025, MNRAS, 538, 605, doi: 10.1093/mnras/staf169

Duvvuri, G. M., Pineda, J. S., Berta-Thompson, Z. K., France, K., & Youngblood, A. 2023, AJ, 165, 12, doi: 10.3847/1538-3881/ac9b49

Ehrenreich, D., Bourrier, V., Bonfils, X., et al. 2012, A&A, 547, A18, doi: 10.1051/0004-6361/201219981

Engle, S. G. 2024, ApJ, 960, 62, doi: 10.3847/1538-4357/ad0840

Fouqué, P., Moutou, C., Malo, L., et al. 2018, MNRAS, 475, 1960, doi: 10.1093/mnras/stx3246

France, K., Froning, C. S., Linsky, J. L., et al. 2013, ApJ, 763, 149, doi: 10.1088/0004-637X/763/2/149

France, K., Duvvuri, G., Egan, H., et al. 2020, AJ, 160, 237, doi: 10.3847/1538-3881/abb465

Gagné, J., & Faherty, J. K. 2018, ApJ, 862, 138, doi: 10.3847/1538-4357/aaca2e

Gaia Collaboration, Brown, A. G. A., Vallenari, A., et al. 2021, A&A, 649, A1, doi: 10.1051/0004-6361/202039657

Gaidos, E., Mann, A. W., Lépine, S., et al. 2014, MNRAS, 443, 2561, doi: 10.1093/mnras/stu1313

Glebocki, R., & Gnacinski, P. 2005,, VizieR On-line Data Catalog: III/244. Originally published in: 2005csss...13..571G

Greatorex, H. J., Milligan, R. O., & Chamberlin, P. C. 2023, ApJ, 954, 120, doi: 10.3847/1538-4357/acea7f

Gunár, S., Schwartz, P., Koza, J., & Heinzel, P. 2020, A&A, 644, A109, doi: 10.1051/0004-6361/202039348
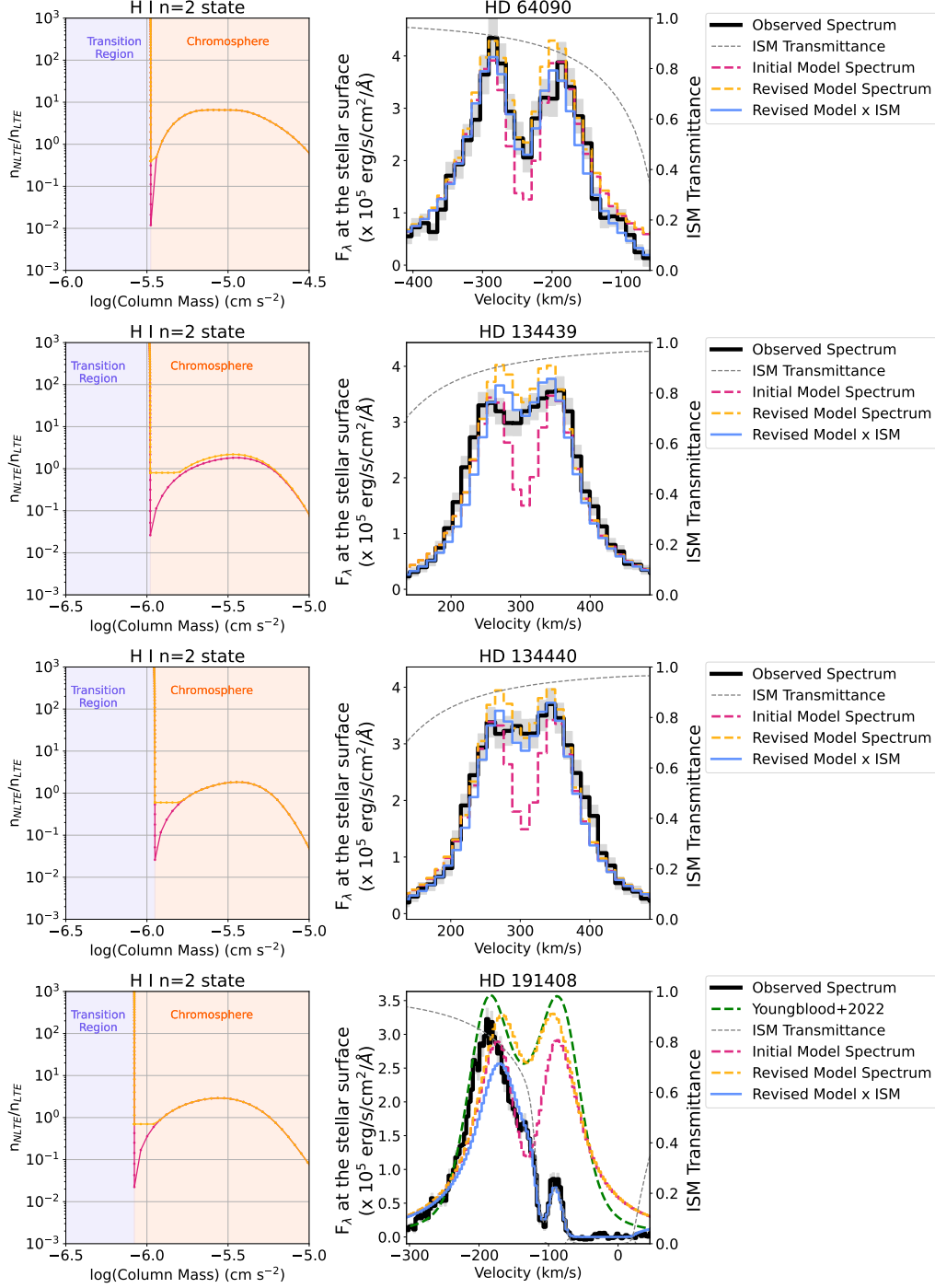
Figure 9. *Left*: n_{NLTE} /n_{LTE} for hydrogen in the n=2 state versus column mass zoomed in to show detail in the transition region and upper chromosphere (these values go to 1 deep in the atmosphere). Initial models are shown in pink, revised models with an imposed minimum set at the boundary between these layers is shown in orange. *Right*: Lyα profiles. HST/STIS observations are plotted in black, with associated errors shaded in gray. The ISM transmittance curve for each star is plotted as a gray dashed line. Initial intrinsic PHOENIX model profiles are plotted in pink and show deep central reversals. Revised intrinsic PHOENIX model profiles are plotted in orange. The revised intrinsic PHOENIX model, after being multiplied by the ISM transmittance curve, is plotted in blue — this profile should match the observations. Stars shown in this figure are (from top to bottom): HD 64090 (K0), HD 134439 (K1), HD 134440 (K2), and HD 191408 (K2.5). We include a comparison to the intrinsic Lyα profile computed in A. Youngblood et al. 2022 for HD 19148, plotted in green.
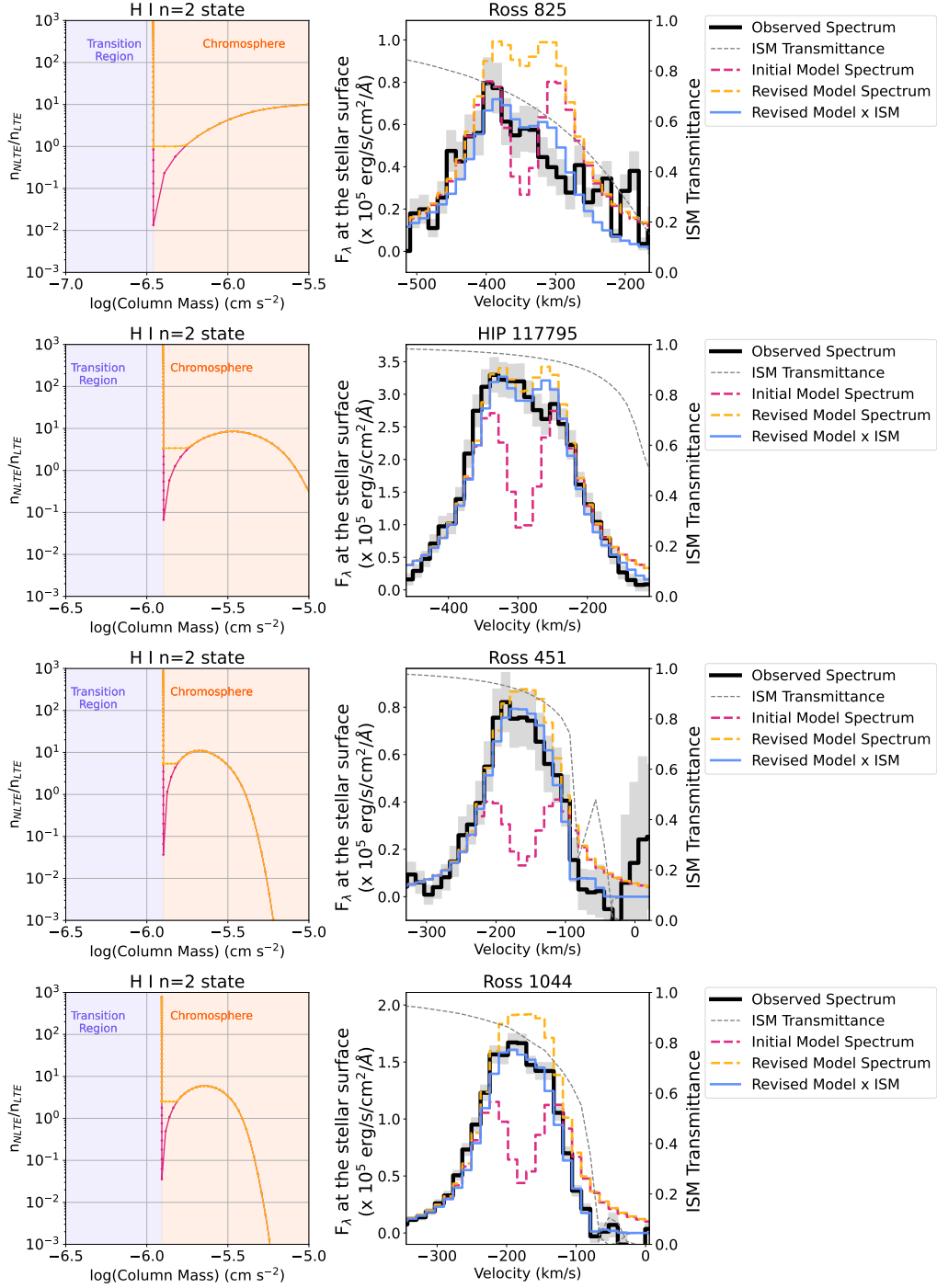
Figure 10. *Same as Figure 9.* Stars shown in this figure are (from top to bottom): Ross 825 (K3), HIP 117795 (K8), Ross 451 (M0), and Ross 1044 (M0).
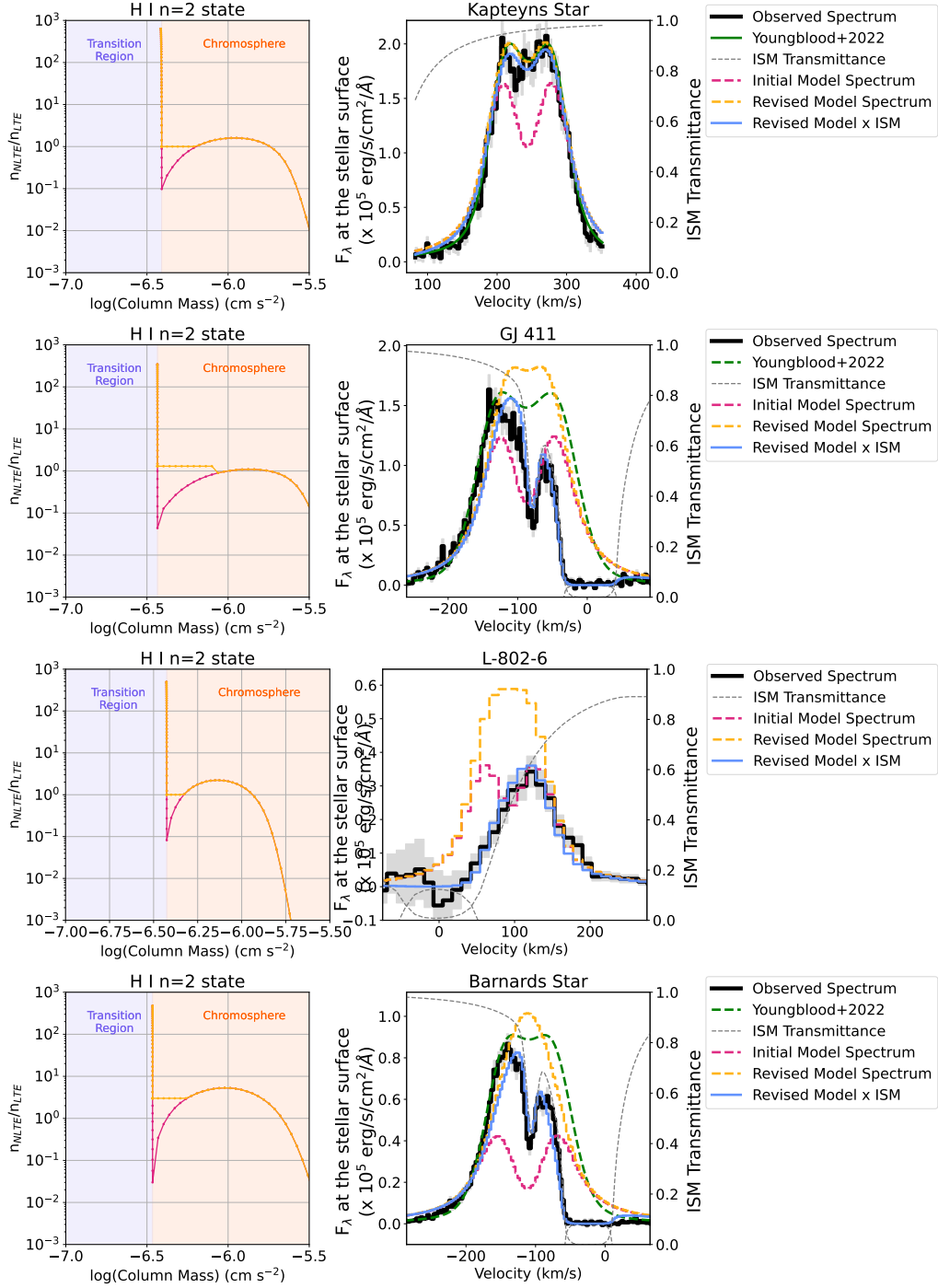
Figure 11. *Same as Figure 9.* Stars shown in this figure are (from top to bottom): Kapteyn's Star (M1), GJ 411 (M2), L-802-6 (M3), Barnard's Star (M4). We include comparisons to the intrinsic Lyα profiles computed in A. Youngblood et al. 2022 for Kapteyn's Star, GJ 411, and Barnard's Star, plotted in green.

Harada, C. K., Dressing, C. D., Kane, S. R., & Ardestani, B. A. 2024, ApJS, 272, 30, doi: 10.3847/1538-4365/ad3e81

Hauschildt, P. H. 1993, JQSRT, 50, 301, doi: 10.1016/0022-4073(93)90080-2

Hauschildt, P. H., & Baron, E. 2006, A&A, 451, 273, doi: 10.1051/0004-6361:20053846

Houdebine, E. R. 2010, A&A, 509, A65, doi: 10.1051/0004-6361/200811602

Isaacson, H., & Fischer, D. 2010, ApJ, 725, 875, doi: 10.1088/0004-637X/725/1/875

Johnstone, C. P., Bartel, M., & Güdel, M. 2021, A&A, 649, A96, doi: 10.1051/0004-6361/202038407

Jönsson, H., Holtzman, J. A., Allende Prieto, C., et al. 2020, AJ, 160, 120, doi: 10.3847/1538-3881/aba592

Kesseli, A. Y., Kirkpatrick, J. D., Fajardo-Acosta, S. B., et al. 2019, AJ, 157, 63, doi: 10.3847/1538-3881/aae982

Kimble, R. A., Woodgate, B. E., Bowers, C. W., et al. 1998, ApJL, 492, L83, doi: 10.1086/311102

Kopparapu, R. K., Ramirez, R. M., SchottelKotte, J., et al. 2014, ApJL, 787, L29, doi: 10.1088/2041-8205/787/2/L29

Kowalska-Leszczynska, I., Bzowski, M., Sokół, J. M., & Kubiak, M. A. 2018, ApJ, 868, 49, doi: 10.3847/1538-4357/aae70b

Lean, J. L., & Repoff, T. P. 1987, J. Geophys. Res., 92, 5555, doi: 10.1029/JD092iD05p05555

Lépine, S., Hilton, E. J., Mann, A. W., et al. 2013, AJ, 145, 102, doi: 10.1088/0004-6256/145/4/102

Linsky, J. L. 1980, ARA&A, 18, 439, doi: 10.1146/annurev.aa.18.090180.002255

Linsky, J. L., Fontenla, J., & France, K. 2014, ApJ, 780, 61, doi: 10.1088/0004-637X/780/1/61

Linsky, J. L., France, K., & Ayres, T. 2013, ApJ, 766, 69, doi: 10.1088/0004-637X/766/2/69

Linsky, J. L., & Redfield, S. 2024, SSRv, 220, 32, doi: 10.1007/s11214-024-01064-3

Linsky, J. L., Wood, B. E., Youngblood, A., et al. 2020, ApJ, 902, 3, doi: 10.3847/1538-4357/abb36f

Loyd, R. O. P., & France, K. 2014, ApJS, 211, 9, doi: 10.1088/0067-0049/211/1/9

Loyd, R. O. P., France, K., Youngblood, A., et al. 2018, ApJ, 867, 71, doi: 10.3847/1538-4357/aae2bd

Luck, R. E. 2017, AJ, 153, 21, doi: 10.3847/1538-3881/153/1/21

Maldonado, J., Micela, G., Baratella, M., et al. 2020, A&A, 644, A68, doi: 10.1051/0004-6361/202039478

Melbourne, K., Youngblood, A., France, K., et al. 2020, AJ, 160, 269, doi: 10.3847/1538-3881/abbf5c

Milligan, R. O., Hudson, H. S., Chamberlin, P. C., Hannah, I. G., & Hayes, L. A. 2020, Space Weather, 18, e02331, doi: 10.1029/2019SW002331

Newton, E. R., Charbonneau, D., Irwin, J., & Mann, A. W. 2015, ApJ, 800, 85, doi: 10.1088/0004-637X/800/2/85

Nordström, B., Mayor, M., Andersen, J., et al. 2004, A&A, 418, 989, doi: 10.1051/0004-6361:20035959

Peacock, S., Barman, T., Shkolnik, E. L., Hauschildt, P. H., & Baron, E. 2019, ApJ, 871, 235, doi: 10.3847/1538-4357/aaf891

Peacock, S., Barman, T. S., Schneider, A. C., et al. 2022, ApJ, 933, 235, doi: 10.3847/1538-4357/ac77f2

Pecaut, M. J., & Mamajek, E. E. 2013, ApJS, 208, 9, doi: 10.1088/0067-0049/208/1/9

Perrin, M. N. 1975, A&A, 44, 9

Redfield, S., & Linsky, J. L. 2008, ApJ, 673, 283, doi: 10.1086/524002

Reggiani, H., & Meléndez, J. 2018, MNRAS, 475, 3502, doi: 10.1093/mnras/sty104

Ribas, I., Tuomi, M., Reiners, A., et al. 2018, Nature, 563, 365, doi: 10.1038/s41586-018-0677-y

Richey-Yowell, T., Shkolnik, E. L., Schneider, A. C., et al. 2023, ApJ, 951, 44, doi: 10.3847/1538-4357/acd2dc

Rosenthal, L. J., Fulton, B. J., Hirsch, L. A., et al. 2021, ApJS, 255, 8, doi: 10.3847/1538-4365/abe23c

Rugheimer, S., Kaltenegger, L., Segura, A., Linsky, J., & Mohanty, S. 2015, ApJ, 809, 57, doi: 10.1088/0004-637X/809/1/57

Sandoval, A., Youngblood, A., Loyd, R. O. P., & France, K. 2023, ApJ, 957, 90, doi: 10.3847/1538-4357/acf6c0

Schneider, A. C., Shkolnik, E. L., Barman, T. S., & Loyd, R. P. 2019, ApJ, 886, 19, doi: 10.3847/1538-4357/ab48de

Shkolnik, E. L., Rolph, K. A., Peacock, S., & Barman, T. S. 2014, ApJL, 796, L20, doi: 10.1088/2041-8205/796/1/L20

Short, C. I., & Doyle, J. G. 1997, A&A, 326, 287

Stanford-Moore, S. A., Nielsen, E. L., De Rosa, R. J., Macintosh, B., & Czekala, I. 2020, ApJ, 898, 27, doi: 10.3847/1538-4357/ab9a35

Stassun, K. G., Oelkers, R. J., Pepper, J., et al. 2018, AJ, 156, 102, doi: 10.3847/1538-3881/aad050

Taylor, A., Dunn, A., Peacock, S., Youngblood, A., & Redfield, S. 2024, ApJ, 964, 80, doi: 10.3847/1538-4357/ad22da

Valenti, J. A., & Fischer, D. A. 2005, ApJS, 159, 141, doi: 10.1086/430500

Waalkes, W. C., Berta-Thompson, Z., Bourrier, V., et al. 2019, AJ, 158, 50, doi: 10.3847/1538-3881/ab24c2

Wielen, R. 1977, A&A, 60, 263

Wilson, D. J., Youngblood, A., Toloza, O., et al. 2022, ApJ, 936, 189, doi: 10.3847/1538-4357/ac87a8

Wood, B. E., Redfield, S., Linsky, J. L., Müller, H.-R., & Zank, G. P. 2005, ApJS, 159, 118, doi: 10.1086/430523

Wylie-de Boer, E., Freeman, K., & Williams, M. 2010, AJ, 139, 636, doi: 10.1088/0004-6256/139/2/636

Youngblood, A., & Newton, E. R. 2025,, v1.1.0 Zenodo, doi: 10.5281/zenodo.15035159

Youngblood, A., Pineda, J. S., Ayres, T., et al. 2022, ApJ, 926, 129, doi: 10.3847/1538-4357/ac4711

Youngblood, A., France, K., Loyd, R. O. P., et al. 2016, ApJ, 824, 101, doi: 10.3847/0004-637X/824/2/101

Youngblood, A., France, K., Loyd, R. O. P., et al. 2017, ApJ, 843, 31, doi: 10.3847/1538-4357/aa76dd

Zacharias, N., Finch, C. T., Girard, T. M., et al. 2012, VizieR Online Data Catalog, I/322A